

Geophysical Research Letters®

RESEARCH LETTER

10.1029/2021GL094295

Key Points:

- Partially coupled climate simulations allow to effectively separate the El Niño–Southern Oscillation (ENSO) and Indian Ocean Dipole (IOD) contributions to Australian precipitation
- Linearly regressing out the IOD influence from the Australian precipitation field leads to an underestimation of the impact of ENSO
- A multivariate regression analysis that uses ENSO and IOD indices to model Australian precipitation variability overestimate the role of IOD

Supporting Information:

Supporting Information may be found in the online version of this article.

Correspondence to:

G. Liguori,
giovanni.liguori@monash.edu

Citation:

Liguori, G., McGregor, S., Singh, M., Arblaster, J., & Di Lorenzo, E. (2022). Revisiting ENSO and IOD contributions to Australian precipitation. *Geophysical Research Letters*, 49, e2021GL094295. <https://doi.org/10.1029/2021GL094295>

Received 11 MAY 2021

Accepted 30 NOV 2021

Author Contributions:

Conceptualization: Giovanni Liguori, Shayne McGregor, Martin Singh, Julie Arblaster, Emanuele Di Lorenzo

Formal analysis: Giovanni Liguori, Martin Singh

Investigation: Giovanni Liguori

Methodology: Giovanni Liguori, Shayne McGregor, Martin Singh, Julie Arblaster, Emanuele Di Lorenzo

Validation: Martin Singh, Julie Arblaster

Visualization: Giovanni Liguori

Writing – original draft: Giovanni Liguori, Shayne McGregor, Martin Singh

Writing – review & editing: Giovanni Liguori, Shayne McGregor, Martin Singh, Julie Arblaster, Emanuele Di Lorenzo

Revisiting ENSO and IOD Contributions to Australian Precipitation

Giovanni Liguori^{1,2} , Shayne McGregor¹ , Martin Singh¹ , Julie Arblaster^{1,3} , and Emanuele Di Lorenzo⁴ 

¹ARC Centre of Excellence for Climate Extremes, Monash University, Clayton, MO, Australia, ²Department of Physics and Astronomy, University of Bologna, Bologna, Italy, ³National Center for Atmospheric Research, Boulder, CO, USA, ⁴Georgia Institute of Technology, Atlanta, GA, USA

Abstract Tropical modes of variability, such as El Niño–Southern Oscillation (ENSO) and the Indian Ocean Dipole (IOD), exert a strong influence on the interannual variability of Australian precipitation. Nevertheless, commonly used indices of ENSO and IOD variability display significant co-variability that prevents a robust quantification of the independent contribution of each mode to precipitation anomalies. This co-variability issue is often addressed by statistically removing ENSO or IOD variability from the precipitation field before calculating teleconnection patterns. However, by performing a suite of coupled and uncoupled modeling experiments in which either ENSO or IOD variability is physically removed, we show that ENSO-only-driven precipitation patterns computed by statistically removing the IOD influence significantly underestimate the impact of ENSO on Australian precipitation variability. Inspired by this, we propose a conceptual model that allows one to effectively separate the contribution of each mode to Australian precipitation variability.

Plain Language Summary It is widely accepted that Tropical modes of variability, such as El Niño–Southern Oscillation (ENSO) and the IOD, play a crucial role in modulating the year-to-year variability in Australian precipitation and extreme weather events, including conditions favorable to record-breaking bushfire events such as the catastrophic 2019–20 Australian bushfire season. However, commonly used indices of ENSO and IOD display a substantial co-variability that prevents a robust quantification of their independent contribution to precipitation anomalies. Over the years several major methodologies have been used to disentangle ENSO and IOD contributions, however, they all present important limitations which prevent the community from reaching a general consensus. Here, we perform a suite of climate simulations to effectively separate ENSO and IOD contributions to Australian precipitation variability. Based on the modeling results, we propose a conceptual model to examine the effects of ENSO on IOD, which is then used to develop an alternative methodology to disentangle ENSO and IOD contribution in both models and observations.

1. Introduction

The strong influence of remote drivers on the Australian climate result in an intraseasonal-to-interannual precipitation variability larger than what is observed in most similar climates elsewhere around the globe (Nicholls, 1997). While extratropical drivers such as the southern annular mode (Hendon et al., 2007) and atmospheric blocking (Pook and Gibson, 1999) exert a notable influence, tropical drivers such as the El Niño–Southern Oscillation (ENSO) and the Indian Ocean Dipole (IOD) have often been reported as the main drivers of Australian precipitation variability on interannual timescales (Pook and Gibson, 1999; Risbey et al., 2009; Ummenhofer et al., 2009), with ENSO primarily affecting north and east Australia throughout the year, and IOD primarily affecting south and east Australia from April to October.

However, while such modes have a large influence over Australian climate, observable quantities used to track ENSO and IOD (i.e., mode indices) often present substantial co-variability (Ashok et al., 2003) that prevents robust quantification of the independent contributions of each mode to rainfall anomalies. Given that the positive phases of ENSO and IOD often co-occur, it is difficult to attribute Australia's observed rainfall anomalies to either of them individually. It is important to clearly state that we separate the physical modes, ENSO and IOD, from observable quantities associated with these modes and used to track their variability, such as the Niño3.4 index (N34; Trenberth, 1997) and the dipole mode index (DMI; Saji et al., 1999).

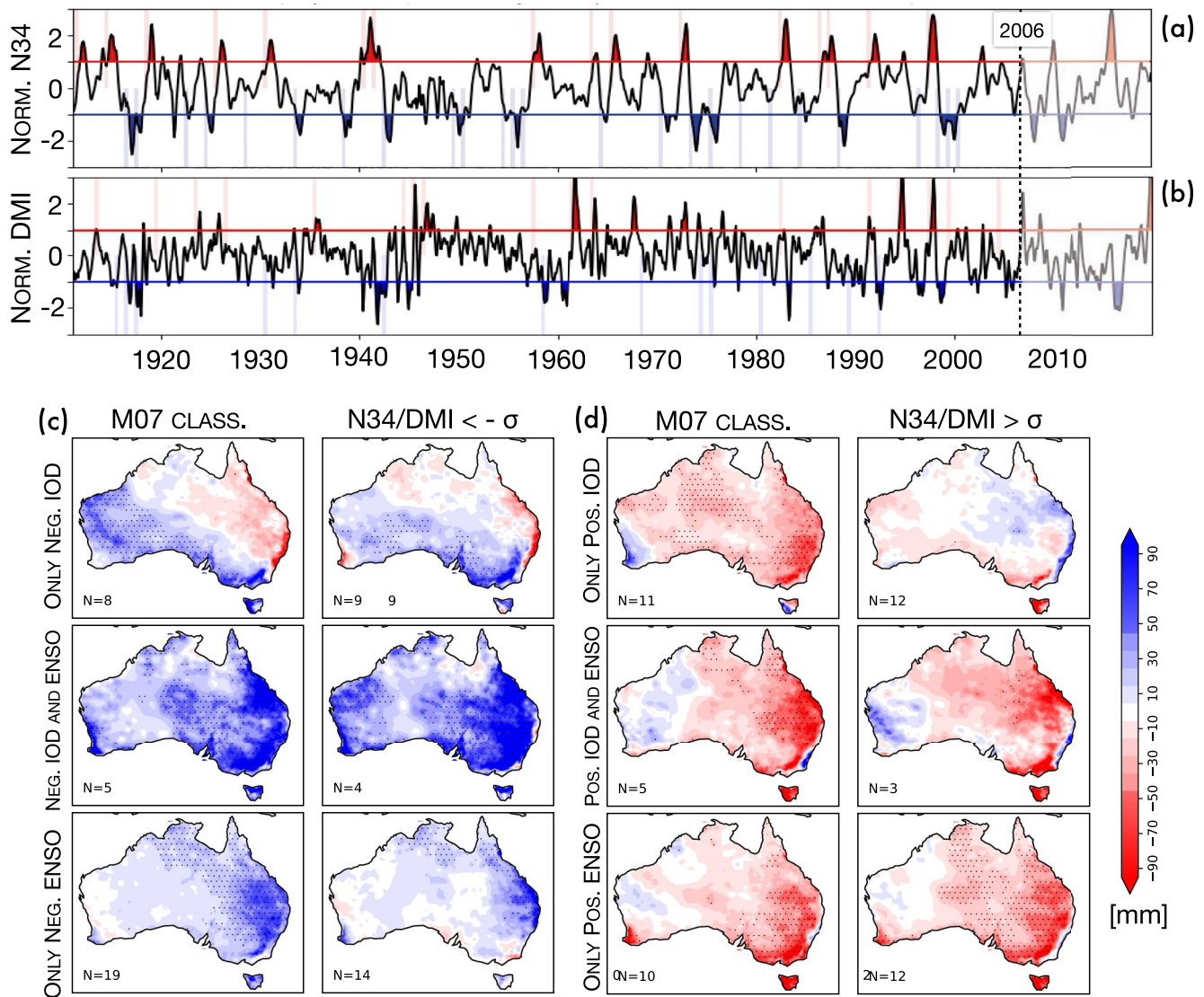


Figure 1. ENSO/IOD classification and impact of precipitation pattern. (a) Normalized time series of Niño3.4 index from 1911 to 2019. The area of above (below) 1 standard deviation is filled in Red (blue) and the vertical red (blue) bars superimposed indicate years classified as positive (negative) El Niño–Southern Oscillation (ENSO) by Meyers et al., 2007 (M07). (b) As in (a) but for dipole mode index time series and IOD events. Lower panel show maps for mean rainfall anomaly (mm) in June–October for ENSO/IOD year types for both (c) Meyers et al. (2007) and (d) 1-STD-threshold classification scheme. The stippling over the maps indicates regions significant at 95% according to a two-tailed Student's t-test.

To overcome the co-variability issue, numerous studies (N. Abram et al., 2008; Lestari and Koh, 2016; Risbey et al., 2009; Ummenhofer et al., 2009; Ummenhofer, Sengupta, Li et al., 2011; Ummenhofer, Sengapat, Briggs et al., 2011; Ummenhofer et al., 2013; Ummenhofer et al., 2015) have used an index for IOD that is by construction linearly independent from ENSO variability. This index, proposed by Meyers et al. (2007) and obtained by performing an intricate procedure involving a lagged Empirical Orthogonal Function (EOF) analysis of a set of pre-processed timeseries, differs from the commonly used DMI as it does not correlate with traditional ENSO indices such as the Niño-3.4 index and the Southern Oscillation Index. As a consequence of this, ENSO- and IOD-driven precipitation patterns obtained using a classification scheme based on Meyer's indices differ from the ones produced for operational purposes by public agencies and private companies, as these are generally calculated from more conventional indices such as Niño indices (Trenberth, 1997) and DMI (see classification comparison of Figures 1a and 1b and table S1 in Supporting Information S1, and composite analysis of Figures 1c and 1d).

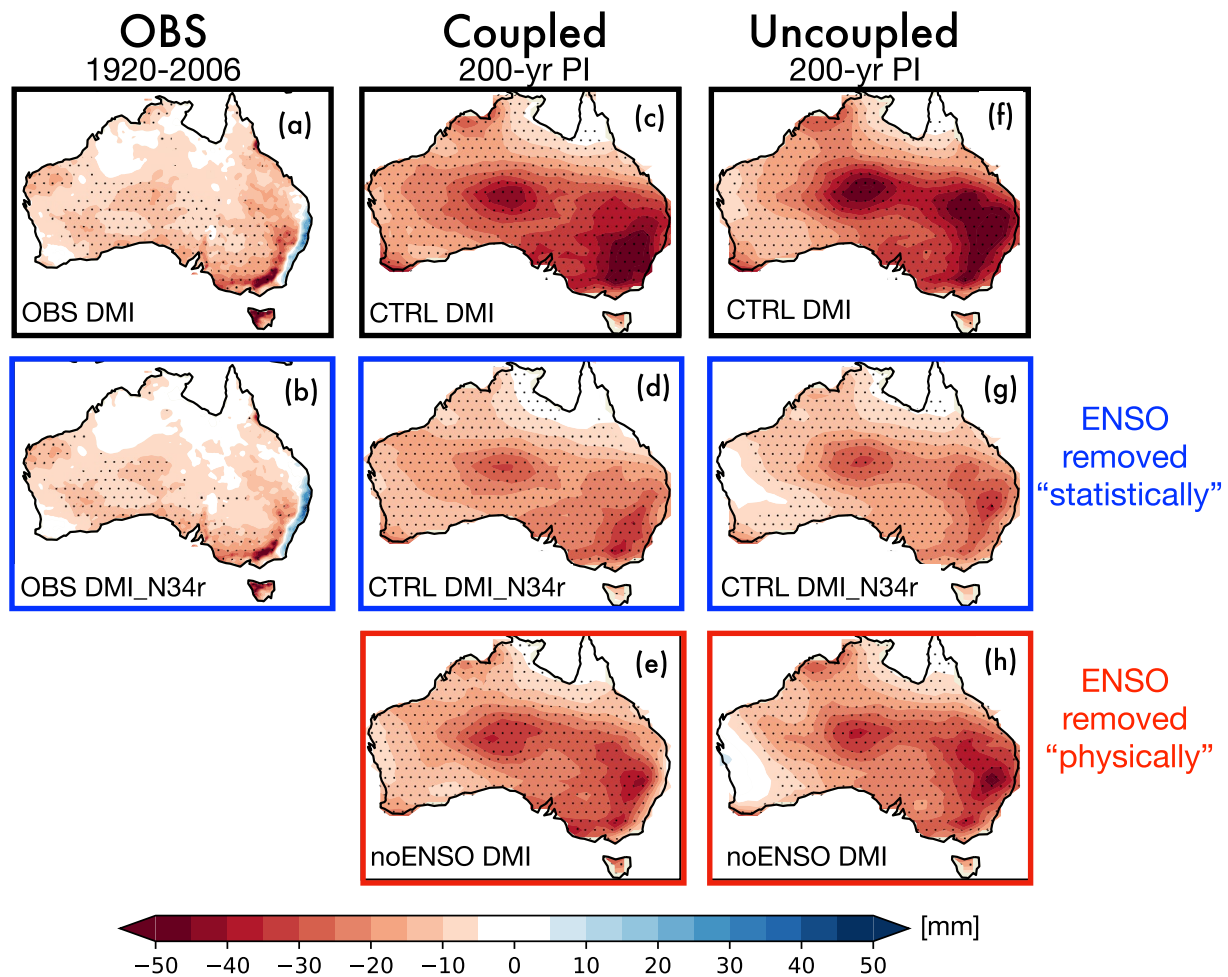


Figure 2. Precipitation patterns associated with variability in dipole mode index (DMI). Top row: DMI index regressed onto mean rainfall anomaly (mm) in June–October for observation (a), the coupled (c) and the uncoupled (f) model simulations. Middle row: as in the top row but for rainfall anomalies in which the variability associated with the Niño3.4 index has been linearly removed. Results for observation (b), coupled (d) and uncoupled (f) control simulations. Bottom row: as in the top row but for the simulations with removed El Niño–Southern Oscillation (ENSO) variability, namely the noENSO-coupled (e) and the noENSO-uncoupled (h) simulations. All the experiments use pre-industrial condition for external forcing. The stippling over the maps indicates regions significant at 95% according to a two-tailed Student's t-test.

In addition to Meyers's methodology, a frequently used technique to disentangle ENSO and IOD contributions to Australian precipitation consists of linearly removing the influence of either ENSO or IOD from the precipitation field before the analysis (partial regression analysis; e.g., Ashok et al., 2003; Cai et al., 2011; Min et al., 2013; Risbey et al., 2009). For instance, a map representing the IOD-only-driven component of Australian precipitation can be obtained by first regressing out the N34 index from the precipitation field, and then regressing the resulting precipitation residual onto the DMI time series (Figure 2b). Analogous calculations but with inverted order produce the ENSO-only-driven precipitation map (Figure 3b). While this "statistical" removal is frequently used to identify ENSO- and IOD-specific teleconnection patterns, there are several shortcomings that are regularly acknowledged in studies that use this method (e.g., Risbey et al., 2009). Specifically, partial regression does not remove potential phase lags and non-linear interaction between the two modes (Cai et al., 2011). Although a recent study suggested a linear theory by which the IOD variability can be explained by ENSO and the seasonal modulation of the Indian Ocean air-sea coupling (Stuecker et al., 2017), non-linearities may be still relevant for the potential effect of IOD on ENSO. Furthermore, by regressing out the ENSO influence from the precipitation, the IOD-driven variability that is correlated with ENSO but not physically caused by it is also removed. It is noteworthy that despite the strong influence that ENSO and IOD have on the Australian Climate, there is no scientific consensus on how to calculate their teleconnection patterns.

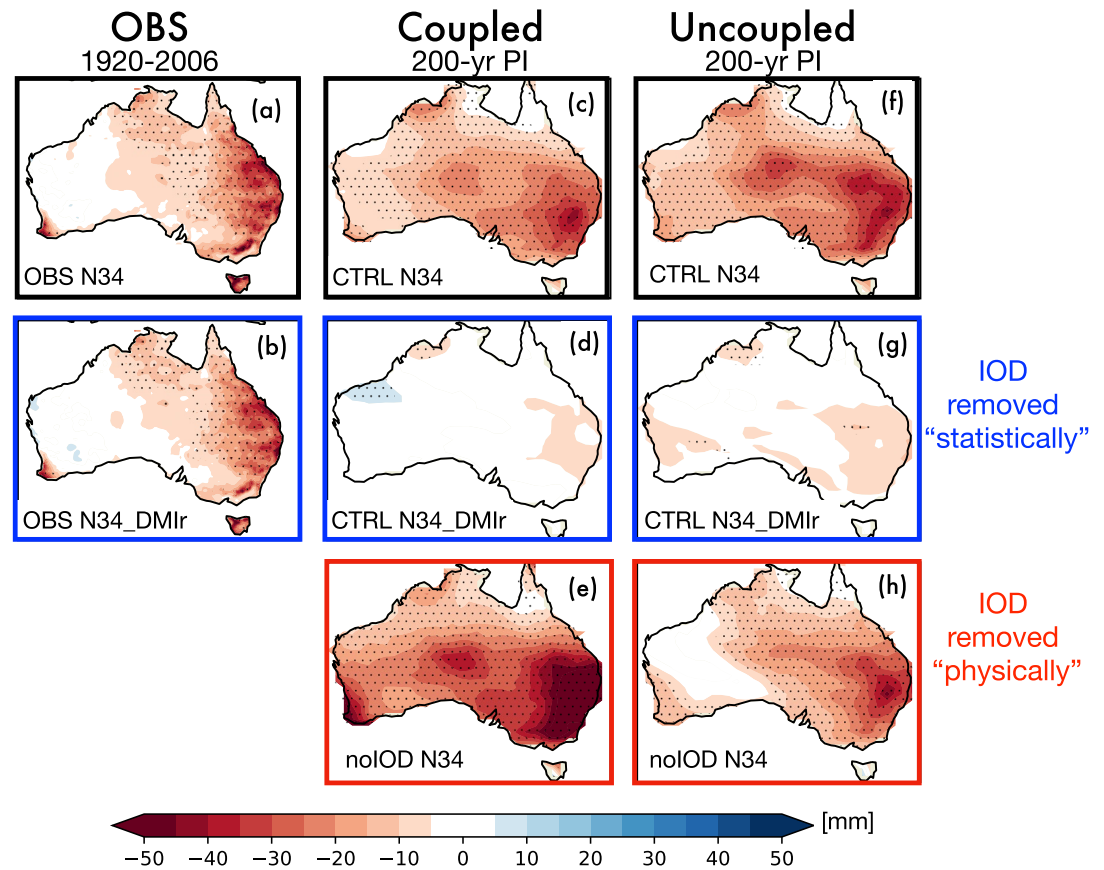


Figure 3. Precipitation patterns associated with variability in Niño3.4. Top row: dipole mode index (DMI) index regressed onto mean rainfall anomaly (mm) in June–October for observation (a), the coupled (c) and the uncoupled (f) model simulations. Middle row: as in the top row but for rainfall anomalies in which the variability associated with the DMI index has been linearly removed. Results for observation (b), coupled (c) and uncoupled (f) simulations. Bottom row: as in the top row but for the simulations with removed Indian Ocean Dipole (IOD) variability, namely the noIOD-coupled (e) and the noIOD-uncoupled (h) simulations. All the experiments use pre-industrial condition for external forcing. The stippling over the maps indicates regions significant at 95% according to a two-tailed Student's t-test.

In this study, we use climate model simulations to motivate a new conceptual framework for the interaction between measurable indices tracking ENSO and IOD variability (e.g., Saji et al., 1999; Trenberth, 1997), and we propose a methodology that produces more robust attribution for the ENSO- and IOD-driven precipitation components. We focus our study on the June–October period as these are the months in which both ENSO and IOD impact the precipitation over Australia the most (Risbey et al., 2009). In addition, we are interested in ENSO-IOD co-variability, and these are the months in which the correlation between N34 and DMI is the highest (Figure S1 in Zhao et al., 2019, doi: 10.1029/2019GL084196). By performing a suite of coupled and uncoupled (atmospheric-only) modeling experiments in which the sea surface temperature (SST) variability associated with either ENSO or IOD is suppressed, we offer evidence that ENSO-only-driven precipitation patterns computed by statistically removing the IOD influence leads to a significant underestimation of the impact of ENSO on Australian precipitation variability. Conversely, our results suggest that the IOD teleconnection computed by regression of the DMI index on to the June–October mean precipitation anomaly overestimates the role of this Indian Ocean mode in Australian variability. As a result of this, we propose a new conceptual framework to separate ENSO and IOD contribution to Australian precipitation.

2. Observations and Modeling Experiments

We use observational SST estimates from the National Oceanic and Atmospheric Administration Extended Reconstruction SST, version 5 (ERSST v5) product (Huang et al., 2017) consisting of monthly mean values from 1854 to the present on a $2^\circ \times 2^\circ$ horizontal grid globally. In addition, to explore the uncertainty in the ERSSTv5 estimates shown in Figure S5 in Supporting Information S1, we compare this data set to the Met Office Hadley Center SST, version 1.1 (HadISST v1.1), which provides monthly estimates from 1870 to the present on a $1^\circ \times 1^\circ$ horizontal grid globally. The comparison indicates that the uncertainty in observational SST products used to calculate the ENSO and IOD indices is relatively small and becomes negligible for Niño indices calculated after 1960 (e.g., Figure S5 in Supporting Information S1).

To track ENSO variability, we use the Niño-3.4 index, which is defined as the area-averaged SST anomaly in the Tropical Pacific region (120°W – 170°W , 5°S – 5°N). For IOD variability we use the DMI, which is defined as in the seminal work of Saji et al. (1999), that is as the difference between the area-averaged SST anomalies in the western Indian Ocean (50°E – 70°E , 10°S – 10°N) and the eastern Indian Ocean (90° – 110°E , 10°S to equator). Observed precipitation estimates come from the Australian Water Availability Project (Jones et al., 2009) which provides a gridded product for the Australian continent at a spatial resolution of $0.05^\circ \times 0.05^\circ$ from 1900 to the present.

All the modeling experiments discussed in this manuscript use Community Earth System Model (CESM) version 1, with the Community Atmosphere Model, version 5 (CESM1-CAM5 Hurrell et al., 2013) at approximately $1^\circ \times 1^\circ$ horizontal resolution in all model components. We analyze six experiments performed under pre-industrial forcing conditions, three partially coupled runs and three atmosphere-only runs. Except the 2200-year long coupled control run (i.e., CTRL-coupled), for which the first 400 years are discarded as spin-up period, all other experiments span 200 years and are initialized from the coupled control at the year 801. Except where otherwise stated, all modelling analysis is performed on the 200-year period 801–1000. While longer simulations are always desirable, a 200-year period provides enough years to simulate the multi-decadal variability present in the observations.

The partially coupled experiments include a full dynamical ocean, but they are run with the SSTs restored to the model monthly mean climatology of CTRL-coupled in specified regions following Liguori and Di Lorenzo (2019). Here, we consider two different restoring masks: the first covers a region in the eastern Pacific (180°W to the American coast, 20°S – N) to remove the SST imprint of ENSO variability (noENSO-coupled experiment), and the second covers a region in the Indian and west Pacific oceans (from the African coast to the maritime continent, 20°S to Asian coast; See Figure S1a in Supporting Information S1) to remove the SST imprint of IOD variability (noIOD-coupled experiment). The model (i.e., CESM1) and the mask utilized for the noENSO-coupled experiment have been already used in previous studies with the explicit intent of controlling or conditioning ENSO variability (e.g., Deser, Simpson et al., 2017; Deser, Guo et al., 2017). The mask utilized for the noIOD-coupled experiment was inspired by two recent studies that used nudged-SST simulations with CESM1 to investigate the variability in the Indian Ocean region (Zhang et al., 2019) and the Southern Hemisphere (Yang et al., 2020). Here, we use a similar Indian Ocean mask, but, in order to avoid any direct effect on the Pacific basin, we limit its eastward extent to the maritime continent, rather than extending it to the dateline (180°W) as done in Zhang et al., 2019 and Yang et al., 2020 (Figure S1 in Supporting Information S1). Throughout the manuscript, monthly mean anomalies are computed by removing the climatological seasonal cycle (i.e., long-term monthly mean of the record analyzed) from detrended fields, which are obtained by removing the linear trend at each grid point.

3. Results

3.1. IOD-Driven Precipitation Variability

We performed a suite of climate model simulations to test if the statistical removal of ENSO via partial regression analysis is an effective way to isolate the IOD-only-driven precipitation variability over the Australian region. Using pre-industrial forcing conditions, the CESM version 1 (Hurrell et al., 2013) was run for 200 years while restoring (2 days restoring timescale) the SSTs to the model monthly mean climatology in the eastern tropical Pacific (15°S – 15°N , 180°W to the coast of South America, with a linearly tapering buffer zone of 5° in all

directions), namely where ENSO signature is the strongest (Figure S1b in Supporting Information S1). The localized SST restoring suppresses ENSO variability while leaving the rest of the model's coupled climate system free to evolve. In this simulation (hereafter, noENSO-coupled) ENSO is "physically removed," in contrast to the partial regression technique in which ENSO is "statistically removed."

Although the restoring is not applied over the Indian Ocean basin, the suppression of SST variability in the eastern tropical Pacific decreases the variance of the monthly mean DMI index by about 30% (Figure S1c in Supporting Information S1). While this effect reveals and confirms important characteristics of the relationship between measurable indices associated with the two modes (i.e., N34 and DMI indices), namely that SST variability in the ENSO region energizes the IOD system (e.g., Cai et al., 2019; Le and Bae, 2019; Stuecker et al., 2017; Zhao et al., 2019), it also introduces differences with our reference simulation (CTRL-coupled) that complicate interpretation. Ideally, to separate the direct contribution of the IOD teleconnection to Australian precipitation, one would like to remove ENSO variability without significantly perturbing the IOD mode. For this reason, the coupled simulation has been complemented with a series of atmosphere-only simulations that use SSTs generated from the coupled control simulation. The first of these, hereafter titled the uncoupled control (CTRL-uncoupled), uses time-dependent SSTs everywhere. The second of these experiments, the noENSO-uncoupled, suppresses ENSO variability by replacing time-dependent SST with the monthly climatology in the eastern tropical Pacific (Figure S1b in Supporting Information S1).

Despite the generally stronger than observed negative regression coefficient, it is noteworthy that both control simulations capture the main features of the observed regression map, namely higher negative coefficient around the center, the south, and the southeast of Australia (Figures 2a, 2c and 2f). The most significant difference with respect to the observation is the lack of a narrow fringe of positive anomaly developing meridionally along the southern part of the eastern coast (Figures 2a and 2b). While further investigations are needed, we speculate that this bias might be linked to poor representation of the orography and to inability of the model to resolve circulations generating precipitation in this area. It is crucial to note that the differences between observations and control simulations cannot be simply reconciled by accounting for the multi-decadal climate variability in the model (Figure S7 and S8 in Supporting Information S1).

A comparison of IOD-only-driven precipitation patterns obtained by removing the influence of ENSO from the precipitation both "statistically" and "physically" show small differences in coupled simulations (Figure 2d vs. 2e; See Figure S2 in Supporting Information S1 for differences) and little changes in uncoupled simulations (Figure 2g vs. 2h; See Figure S2 in Supporting Information S1 for differences). Regardless of the coupling, regressing out the N34 index seems to approximate well the "physical" removal of ENSO variability simulated in the noENSO runs. We do note that small but robust differences are visible between coupled and uncoupled runs: while both control simulations share the exact same DMI index and present very similar regression maps (Figures 2c and 2f), the removal of ENSO, either "statistically" or "physically," results in a negative regression coefficient over western Australia only for the coupled runs

3.2. ENSO-Driven Precipitation Variability

Similar to the experiments with suppressed ENSO variability, we perform simulations in which the IOD variability is suppressed either by either restoring (for the coupled run; noIOD-coupled) or prescribing (for the uncoupled run; noIOD-uncoupled) the SSTs in the Indian Ocean basin (from 20°S to the Asian continent, and from the African coastline to the eastern limits of the Maritime continent; Figure S1a in Supporting Information S1) to the monthly mean climatology of the coupled control run (i.e., CTRL-uncoupled).

While experiments with suppressed ENSO variability suggest that the partial regression technique effectively isolates the IOD-only-driven precipitation component from ENSO variability, runs with suppressed IOD variability (i.e., noIOD-coupled and noIOD-uncoupled) reveal anomaly patterns for ENSO-only-driven precipitation component that are highly sensitive to the methodology used to remove IOD variability ("statistical" vs. "physical" removal; Figures 3d vs. 3e and 3g vs. 3h; See Figure S3 in Supporting Information S1 for differences). While, simulations with suppressed IOD variability have large ENSO regression coefficients, precipitation residuals obtained regressing out the DMI signal ("statistical" removal) have very weak (near-zero) ENSO regression coefficients regardless of the coupling (Figures 3d and 3g). This suggests that in the attempt to "statistically" remove the IODs influence on precipitation, a substantial fraction of ENSO variability has also been removed. It

is noteworthy that the noIOD-coupled simulation presents a regression coefficient for the standardized N34 index that is significantly larger than what is found in the coupled control simulation. This unexpected result can be explained by noting that the variance of ENSO increases significantly (the variance of the N34 index increases of ~45%) by suppressing the SST variability in the Indian Ocean basin, which supports recent results (e.g., Kajtar et al., 2017; Terray et al., 2016) suggesting that variability in the Indian Ocean acts to damp ENSO variability.

The "statistical" removal of IOD variability has a clear effect in the CTRL simulations (both coupled and uncoupled) but not in observations, where the N34 regression coefficient spatial pattern remains and is only marginally weaker (Figures 3a and 3b). This is in part explained by noting the lower than modeled correlation coefficient between N34 and DMI (0.19 and 0.59, for observations and model respectively). While this may indicate a misrepresentation of the IOD-ENSO relationship in the model, high N34-DMI correlation coefficients, like those modeled, have been observed in more recent periods and appear to arise in part from natural variability (Figure S4a in Supporting Information S1). The weaker the correlation, the better the accuracy of the "statistical" removal with partial regression analysis.

3.3. A Conceptual Model for the Correlation Between ENSO and Indian Ocean Dipole Indices

Our partially coupled simulations indicate that the partial regression analysis does not effectively isolate the ENSO-only-driven component of Australian precipitation variability. While, "physically" removing IOD variability appears to be the method of choice in models, it is not applicable to the observations, where statistical analysis is the only available option. However, findings on the relationship between indices of ENSO and IOD that are inferred from our coupled experiments can be exploited to build a conceptual and statistical model for the precipitation variability over Australia. The noENSO-coupled run suggests that SST variability in the Niño3.4 region energizes and modulates the SST variability in the DMI region, and the noIOD-coupled run indicates that the Indian Ocean variability acts as a damping mechanism for ENSO, at least when this mode is tracked by an SST-based index such as the Niño3.4. However, the damping effect that the Indian Ocean variability has on ENSO should not necessarily be interpreted as if the IOD mode has a direct impact on the N34 timeseries. The suppression of the Indian Ocean variability might favor the growth of ENSO's SST anomalies through dynamics unrelated to IOD variability, for example, by limiting the dissipation of ENSO-induced atmospheric anomalies in the Indian Ocean. Therefore, to develop a simple conceptual model, we begin with the assumption that the N34 timeseries is independent from IOD variability. Furthermore, let us assume that ENSO and IOD are truly independent modes and that the positive correlation between N34 and DMI is the result of the difficulty (perhaps impossibility) of tracking IOD variability without "measuring" ENSO at the same time. Although previous studies have noted the two-way coupling between ENSO and IOD (N J Abram et al., 2020; Ha et al., 2017; Izumo et al., 2010; Jourdain et al., 2016; Santoso et al., 2012), we will show that a robust quantification of the contribution of each mode to Australian precipitation is possible by neglecting the possible influence of IOD on ENSO.

Given the above assumptions, we can elaborate on a simple statistical model for the June–October mean precipitation $P(x,y,t)$ that is based on unobserved independent time series of ENSO and IOD, $ENSO(t)$ and $IOD(t)$:

$$P(x, y, t) = b1(x, y) * ENSO(t) + b2(x, y) * IOD(t) + N(x, y, t) \quad (1)$$

where, $b1(x, y)$ and $b2(x, y)$ are spatially varying coefficients modeling the impact of ENSO and IOD, respectively, and the term $N(x, y, t)$ represents the precipitation variability unexplained by the first two terms (i.e., residual term). If all the time series in (1), $P(x, y, t)$, $ENSO(t)$, $IOD(t)$ and $N(t)$, are standardized to have variance equal to one, then the square of the coefficients, $b1(x, y)^2$ and $b2(x, y)^2$, sum to one for each (x,y) point. Consistent with the assumption that the DMI index spuriously tracks some of the variability associated with ENSO, we write the "measurable" N34 and DMI time series as follow:

$$N34(t) = ENSO(t) \quad (2a)$$

$$DMI(t) = \alpha ENSO(t) + \sqrt{1 - \alpha^2} IOD(t) \quad (2b)$$

where, α defines the fraction of ENSO variability that "leaks" onto the DMI index and can be approximated with the correlation coefficient between N34 and DMI. Note that the square of the coefficient terms in (2b), α and $\sqrt{1 - \alpha^2}$, sum to one and have been obtained assuming that $DMI(t)$ is also standardized. Equations 2a and 2b

represent the core of our conceptual model and will be used to develop a methodology to isolate the independent contribution of ENSO and IOD to precipitation anomalies that is alternative to partial regressions (Ashok et al., 2003; Cai et al., 2011; Min et al., 2013; Risbey et al., 2009) or Meyer's decomposition method (Meyers et al., 2007). Despite their simplicity, Equations 2a and 2b seem to give a plausible representation of the relationship among the physical modes ENSO and IOD and their respective indices N34 and DMI during June–October. For instance, while the SST regression maps of the DMI and IOD timeseries are essentially identical in the Indian Ocean, the signature of ENSO, clearly visible in the SST regression map of the DMI index, does not appear when one regresses SST on the timeseries of IOD(t) (See also Figure S6 in Supporting Information S1). The latter timeseries represents the SST signature of the physical IOD mode according to our conceptual model.

While, Equation 1 is a valid conceptual model, it is based on unobservable variables and does not allow for calculations of ENSO and IOD contributions on precipitation variability. However, the statistical model of Equation 1 can be written in terms of the observable time series $N34(t)$ and $DMI(t)$ as follows:

$$P(x, y, t) = B1(x, y) * N34(t) + B2(x, y) * DMI(t) + N(x, y, t) \quad (3)$$

where, $B1(x,y)$ and $B2(x,y)$ have analogous meanings to the matching terms in (Equation 1). By equating (Equation 3) and (Equation 1), and using (Equation 2a) and (Equation 2b) to replace unobservable ENSO and IOD time series, it is possible to derive an expression for $b1(x,y)$ and $b2(x,y)$ in terms of $B1(x,y)$ and $B2(x,y)$:

$$b1(x, y) = B1(x, y) + \alpha B2(x, y) \quad (4a)$$

$$b2(x, y) = B2(x, y) * \sqrt{1 - \alpha^2} \quad (4b)$$

$B1(x,y)$ and $B2(x,y)$ are linked to our "measurable" time series and can be estimated by treating (Equation 3) as a multi-linear regression problem, that is finding $B1(x,y)$ and $B2(x,y)$ such that the residual term in (1) is minimized. Equations 4a and 4b represent a practical way to estimate ENSO and IOD independent contributions while accounting for the correlation between their "measurable" indices (e.g., DMI and N34). The proposed method is alternative to Meyer's EOF-based decomposition and differs from it mostly because of its conceptual simplicity and direct accounts for ENSOs effect on DMI. The conceptual model is based on the physical assumption that the effect of ENSO on SST variability in the Indian Ocean is large compared to the corresponding effect of the IOD on SST variability in the Eastern Pacific.

Using June–October mean values for precipitation anomalies, and the N34 and DMI indices, we estimated the terms $B1(x,y)$ and $B2(x,y)$, and from there the terms $b1(x,y)$ and $b2(x,y)$, which quantify the independent contribution of ENSO and IOD to the interannual precipitation variability over Australia, respectively. Estimates of these spatial coefficients for both the observations and the coupled control simulation reveals similarities as well as fundamental differences (Figure 4). For the observations, the weak correlation between N34 and DMI during June–October ($\alpha = 0.19$ for 1920–2018) results in both N34 and DMI regression coefficients (i.e., $b1(x,y)$ and $b2(x,y)$) being very similar to the maps of ENSO and IOD independent contributions (i.e., $B1(x,y)$ and $B2(x,y)$). In fact, when α approaches zero $b1(x,y)$ and $b2(x,y)$ tend to $B1(x,y)$ and $B2(x,y)$, respectively. However, since α changes over time and has become larger in recent decades (Figure S4a in Supporting Information S1), these α -based corrective factors in (4a) and (4b) (i.e., " $+ \alpha B2(x, y)$ " and " $\varepsilon * \sqrt{1 - \alpha^2}$ ") become appreciable when the same analysis is repeated for the last available 30 years period (See Figure S4b in Supporting Information S1).

The relevance of these corrective factors is evident for the coupled control simulation where N34 index and DMI are more tightly connected (i.e., $\alpha = 0.59$ over the 200-year control period). In fact, while the N34 coefficients ($B1(x,y)$; Figure 4e) present a weak east-west dipole structure with negative values in the east and positive in the west, the ENSO-only-driven precipitation pattern ($b1(x,y)$; Figure 4f) depicts a negative monopole structure with the largest anomaly located over the southeast. Furthermore, the spatial structure of the DMI coefficients ($B2(x, y)$; Figure 4e) is similar to the IOD-only-driven precipitation pattern ($b2(x, y)$; Figure 4h) but with anomalies that are appreciably increased in size. In conclusion, the α -based corrective factors both amplify and reduce ENSO and IOD teleconnection patterns, respectively.

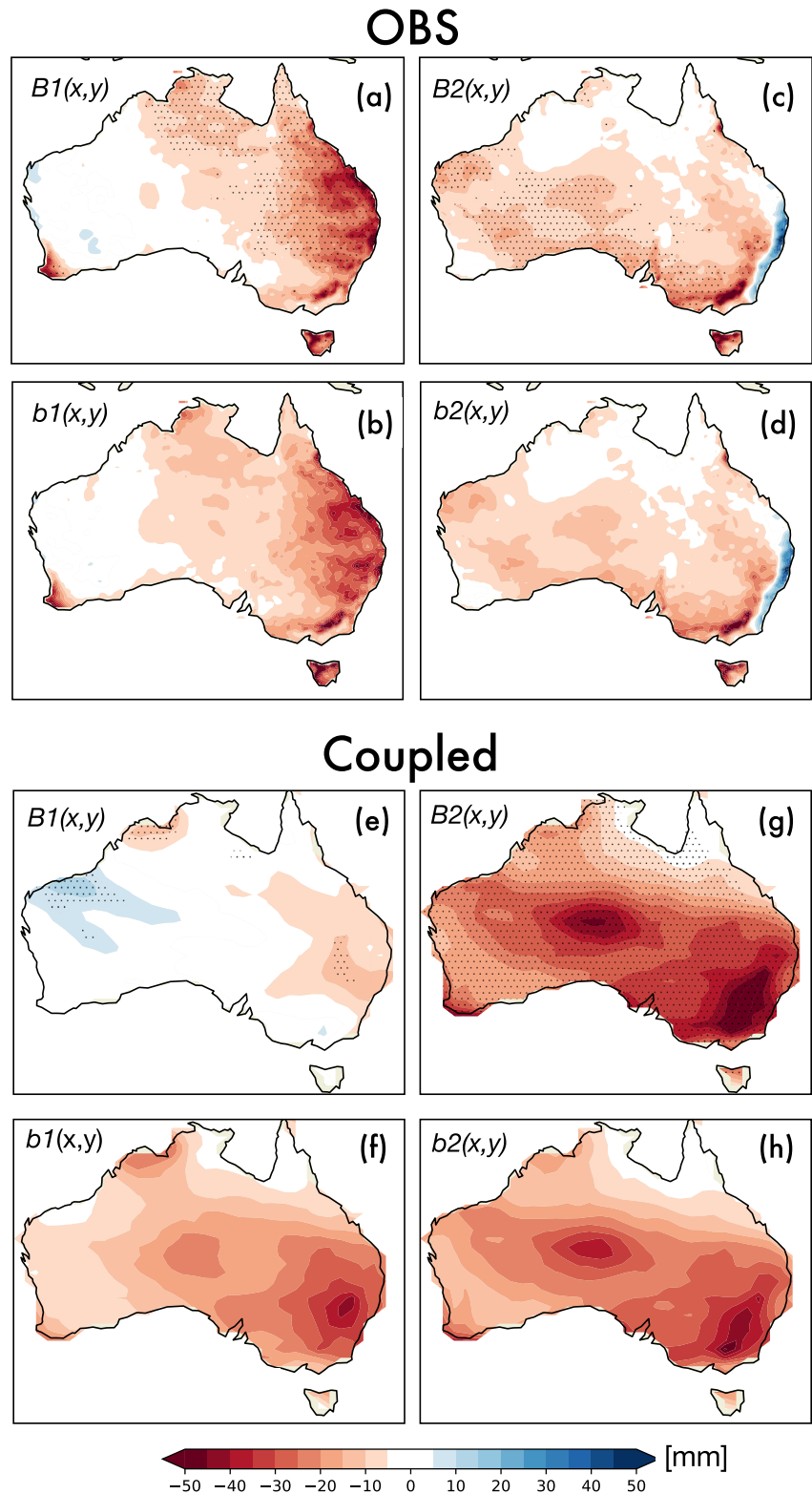


Figure 4. Multi-linear regression model for JJASO mean precipitation based on N34 and dipole mode index (DMI). The ENSO-only and IOD-only driven precipitation components, $b_1(x,y)$ and $b_2(x,y)$ respectively, are obtained as a linear combination (see main text for a detailed description) of the multi-linear regression maps associated with N34(t) and DMI(t) contributions, $B_1(x,y)$ and $B_2(x,y)$, respectively. Results shown for both observations (a–d) and coupled simulations (e–h). The stippling over $B_1(x,y)$ and $B_2(x,y)$ maps indicates regions significant at 95% according to a two-tailed Student's t-test.

4. Summary and Discussion

Using a suite of climate model simulations, we offer evidence that ENSO-driven precipitation patterns obtained by "statistically" removing the IOD influence (tracked by the DMI) from precipitation anomalies leads to a significant underestimation of the impact of ENSO on Australian precipitation variability. Simulations in which the Indian Ocean's influence on the climate system is "physically" removed present an ENSO-driven precipitation pattern substantially stronger than the one obtained with the statistical removal. Furthermore, our experiments reveal important relationships between SST variability in the ENSO region (i.e., eastern tropical Pacific) and the tropical Indian Ocean. The variability in the eastern tropical Pacific appears to energize the interannual variability in the Indian Ocean region, including the variability tracked by the DMI time series. On the contrary, variability in the Indian Ocean region appears to have a damping effect on the eastern tropical Pacific, with the variance of the N34 index reduced by 40% when the Indian Ocean air-sea coupling is included in the simulation. Despite the results being consistent with previous studies (e.g., Cai et al., 2019; Le and Bae, 2019; Stuecker et al., 2017; Zhao et al., 2019), the DMI variability is substantially larger than what is observed (Figure S1c in Supporting Information S1). While this bias in the variability might affect the relationship between ENSO and IOD as represented in the model, it is unlikely to produce qualitative changes in our conclusions. Nonetheless, it is important to repeat the experiments once a model with a small or no bias in the DMI variability becomes available. Our idealized modeling setup might also introduce additional uncertainties in the results. For instance, the Indian Ocean mask covers the entire basin resulting in the suppression of more than just IOD-related SST variability. Specifically, the variability associated with the Indian Ocean Basin mode (Klein et al., 1999) is suppressed. This issue may be addressed by limiting the masked area to the region where the IOD is more active, namely the eastern pole in the eastern Indian Ocean and the western pole in the Arabian Sea.

Based on these simulations, we propose a simple statistical model that uses measurable indices of ENSO and IOD modes (i.e., N34 and DMI) to quantify ENSO and IOD-driven precipitation anomalies over Australia. While this model represents a step toward the solution of a complex problem in climate science, namely how to disentangle ENSO and IOD teleconnections using partially covarying mode indices, it must be noted that our simple model has still some deficiencies. In fact, the simple model does not represent the damping effect that Indian Ocean SST variability seems to have on the ENSO system in climate simulations.

It is noteworthy that the simple model produces results that are partially different depending on if it is applied to model simulation or observations (see Figure 4). Specifically, the difference between IOD-only driven precipitation (i.e., $b1[x,y]$) and the DMI regression coefficient ($B1[x,y]$) is much larger in the model simulation. While this difference might suggest a deficiency of the conceptual model, it might also reflect a fundamentally different relationship between N34 and DMI in the climate model. Despite this, we believe that our method represents a valid alternative to both partial regressions and Meyer's methodology for the following reasons: (a) the derivation of ENSO and IOD indices is substantially simpler and does not involve EOF calculations and the removal of decadal variability; (b) indices are derived exclusively from SST fields, hence facilitating their monitoring and interpretation. Both these characteristics make the methodology better suited for operational use. Finally, a benefit of our method is that (c) it explicitly recognizes that some of the DMI variability is indirectly driven by ENSO.

Conflict of Interest

The authors declare no conflicts of interest relevant to this study.

Data Availability Statement

The authors use two SST data sets, the Met Office Hadley Centre SST, version 1.1 (HadISST v1.1, available at <https://www.metoffice.gov.uk/hadobs/hadisst/data/download.html>) data set (Rayner et al., 2003) and the National Oceanic and Atmospheric Administration Extended Reconstruction SST, version 5 (ERSST v5; available at <https://doi.org/10.7289/V5T72FNM>) product (Huang et al., 2017). Data from all CESM1 experiments except the control simulation, which is available on the Earth System Grid (www.earthsystemgrid.org/), are available at <https://doi.org/10.5281/zenodo.5707525>.

Acknowledgments

G. Liguori, S. McGregor, J. Arblaster, and M. Singh acknowledge support from the Australian Research Council through the Centre of Excellence for Climate Extremes (CE170100023). Computational resources and services from the National Computational Infrastructure, which is supported by the Australian Government, are gratefully acknowledged. Portions of this study were supported by the Regional and Global Model Analysis (RGMA) component of the Earth and Environmental System Modeling Program of the U.S. Department of Energy's Office of Biological & Environmental Research (BER) Cooperative Agreement # DE-FC02-97ER62402 and by the National Center for Atmospheric Research, which is a major facility sponsored by the National Science Foundation under Cooperative Agreement No. 1852977. This research used resources from the National Energy Research Scientific Computing Center, a DOE Office of Science User Facility supported by the Office of Science of the U.S. Department of Energy under Contract No. DE-AC02-05CH11231. E. D. Lorenzo and G. Liguori acknowledge the support of the National Science Foundation through the grants NSF-OCE 1634996, NSF-OCE 1419292, and NSF-OCE 1948627. G. Liguori also thanks Alex Sen Gupta and Harry Hendon for insightful discussions in the early stages of this work. All the authors thank the two anonymous reviewers for their constructive comments on the manuscript.

References

Abram, N., Gagan, M., Cole, J., Hantoro, W., & Mudelsee, M. (2008). Recent intensification of tropical climate variability in the Indian Ocean. *Nature Geoscience*, 1(12), 849–853. <https://doi.org/10.1038/ngeo357>

Abram, N. J., Wright, N. M., Ellis, B., Dixon, B. C., Wurtzel, J. B., England, M. H., et al. (2020). Coupling of Indo-Pacific climate variability over the last millennium. *Nature*, 579(7799), 385–392. <https://doi.org/10.1038/s41586-020-2084-4>

Ashok, K., Guan, Z. Y., & Yamagata, T. (2003). A look at the relationship between the ENSO and the Indian Ocean Dipole. *Journal of the Meteorological Society of Japan*, 81(1), 41–56. <https://doi.org/10.2151/jmsj.81.41>

Cai, W., Wu, L., Lengaigne, M., Li, T., McGregor, S., Kug, J.-S., et al. (2019). Pantropical climate interactions. *Science*, 363(6430). <https://doi.org/10.1126/science.aav4236>

Cai, W. J., van Rensch, P., Cowan, T., & Hendon, H. H. (2011). Teleconnection pathways of ENSO and the IOD and the mechanisms for impacts on Australian rainfall. *Journal of Climate*, 24(15), 3910–3923. <https://doi.org/10.1175/2011jcli4129.1>

Deser, C., Guo, R., & Lehner, F. (2017). The relative contributions of tropical Pacific sea surface temperatures and atmospheric internal variability to the recent global warming hiatus. *Geophysical Research Letters*, 44, 7945–7954. <https://doi.org/10.1002/2017GL074273>

Deser, C., Simpson, I. R., McKinnon, K. A., & Phillips, A. S. (2017). The Northern Hemisphere extra-tropical atmospheric circulation response to ENSO: How well do we know it and how do we evaluate models accordingly? *Journal of Climate*, 30, 5059–5082. <https://doi.org/10.1175/JCLI-D-16-0844.1>

Ha, K. J., Chu, J. E., Lee, J. Y., & Yun, K. S. (2017). Interbasin coupling between the tropical Indian and Pacific Ocean on interannual timescale: Observation and CMIP5 reproduction. *Climate Dynamics*, 48(1–2), 459–475. <https://doi.org/10.1007/s00382-016-3087-6>

Hendon, H. H., Thompson, D. W. J., & Wheeler, M. C. (2007). Australian rainfall and surface temperature variations associated with the Southern Hemisphere annular mode. *Journal of Climate*, 20(11), 2452–2467. <https://doi.org/10.1175/jcli4134.1>

Huang, B., Thorne, P., Banzon, V., Boyer, T., Chepurin, G., Lawrimore, J., et al. (2017). Extended reconstructed sea surface temperature, version 5 (ERSSTv5): Upgrades, validations, and intercomparisons. *Journal of Climate*, 30(20), 8179–8205. <https://doi.org/10.1175/jcli-d-16-0836.1>

Hurrell, J. W., Holland, M. M., Gent, P. R., Ghan, S., Kay, J. E., Kushner, P. J., et al. (2013). The community earth system model: A framework for collaborative research. *Bulletin of the American Meteorological Society*, 94(9), 1339–1360. <https://doi.org/10.1175/bams-d-12-00121.1>

Izumo, T., Vialard, J., Lengaigne, M., Montegut, C. D., Behera, S. K., Luo, J. J., et al. (2010). Influence of the state of the Indian Ocean Dipole on the following year's El Niño. *Nature Geoscience*, 3(3), 168–172. <https://doi.org/10.1038/ngeo760>

Jones, D., Wang, W., & Fawcett, R. (2009). High-quality spatial climate data-sets for Australia. *Australian Meteorological and Oceanographic Journal*, 58(04), 233–248. <https://doi.org/10.22499/2.5804.003>

Jourdain, N. C., Lengaigne, M., Vialard, J., Izumo, T., & Sen Gupta, A. (2016). Further insights on the influence of the Indian Ocean Dipole on the following year's ENSO from observations and CMIP5 models. *Journal of Climate*, 29(2), 637–658. <https://doi.org/10.1175/jcli-d-15-0481.1>

Kajtar, J. B., Santoso, A., England, M. H., & Cai, W. J. (2017). Tropical climate variability: Interactions across the Pacific, Indian, and Atlantic Oceans. *Climate Dynamics*, 48(7–8), 2173–2190. <https://doi.org/10.1007/s00382-016-3199-z>

Klein, S. A., Soden, B. J., & Lau, N.-C. (1999). Remote sea surface temperature variations during ENSO: Evidence for a tropical atmospheric bridge. *Journal of Climate*, 12, 917–932. [https://doi.org/10.1175/1520-0442\(1999\)012<0917:rsstvd>2.0.co;2](https://doi.org/10.1175/1520-0442(1999)012<0917:rsstvd>2.0.co;2)

Le, T., & Bae, D. H. (2019). Causal links on interannual timescale between ENSO and the IOD in CMIP5 future simulations. *Geophysical Research Letters*, 46(5), 2820–2828. <https://doi.org/10.1029/2018gl081633>

Lestari, R. K., & Koh, T. Y. (2016). Statistical evidence for asymmetry in ENSO–IOD interactions. *Atmosphere–Ocean*, 54(5), 498–504. <https://doi.org/10.1080/07055900.2016.1211084>

Liguori, G., & Di Lorenzo, E. (2019). Separating the North and south Pacific meridional modes contributions to ENSO and tropical decadal variability. *Geophysical Research Letters*, 46(2), 906–915. <https://doi.org/10.1029/2018gl080320>

Meyers, G., McIntosh, P., Pigot, L., & Pook, M. (2007). The years of El Niño, La Niña, and interactions with the tropical Indian ocean. *Journal of Climate*, 20(13), 2872–2880. <https://doi.org/10.1175/jcli4152.1>

Min, S. K., Cai, W. J., & Whetton, P. (2013). Influence of climate variability on seasonal extremes over Australia. *Journal of Geophysical Research: Atmospheres*, 118(2), 643–654. <https://doi.org/10.1002/jgrd.50164>

Nicholls, N. (1997). Increased Australian wheat yield due to recent climate trends. *Nature*, 387(6632), 484–485. <https://doi.org/10.1038/387484a0>

Pook, M., & Gibson, T. (1999). Atmospheric blocking and storm tracks during SOP-1 of the FROST Project. *Australian Meteorological Magazine*, 51–60.

Rayner, N. A., Parker, D. E., Horton, E. B., Folland, C. K., Alexander, L. V., Rowell, D. P., et al. (2003). Global analyses of sea surface temperature, sea ice, and night marine air temperature since the late nineteenth century. *Journal of Geophysical Research*, 108(D14), 4407. <https://doi.org/10.1029/2002JD002670>

Risbey, J. S., Pook, M. J., McIntosh, P. C., Wheeler, M. C., & Hendon, H. H. (2009). On the remote drivers of rainfall variability in Australia. *Monthly Weather Review*, 137(10), 3233–3253. <https://doi.org/10.1175/2009mwr2861.1>

Saji, N. H., Goswami, B. N., Vinayachandran, P. N., & Yamagata, T. (1999). A dipole mode in the tropical Indian Ocean. *Nature*, 401(6751), 360–363. <https://doi.org/10.1038/43854>

Santoso, A., England, M. H., & Cai, W. (2012). Impact of Indo-Pacific feedback interactions on ENSO dynamics diagnosed using ensemble climate simulations. *Journal of Climate*, 25(21), 7743–7763. <https://doi.org/10.1175/jcli-d-11-00287.1>

Stuecker, M. F., Timmermann, A., Jin, F. F., Chikamoto, Y., Zhang, W. J., Wittenberg, A. T., et al. (2017). Revisiting ENSO/Indian Ocean Dipole phase relationships. *Geophysical Research Letters*, 44(5), 2481–2492. <https://doi.org/10.1002/2016gl072308>

Terray, P., Masson, S., Prodhomme, C., Roxy, M. K., & Sooraj, K. P. (2016). Impacts of Indian and Atlantic oceans on ENSO in a comprehensive modeling framework. *Climate Dynamics*, 46(7–8), 2507–2533. <https://doi.org/10.1007/s00382-015-2715-x>

Trenberth, K. (1997). The definition of El Niño. *Bulletin of the American Meteorological Society*, 78(12), 2771–2777. [https://doi.org/10.1175/1520-0477\(1997\)078<2771:tdoeno>2.0.co;2](https://doi.org/10.1175/1520-0477(1997)078<2771:tdoeno>2.0.co;2)

Ummenhofer, C. C., England, M. H., McIntosh, P. C., Meyers, G. A., Pook, M. J., Risbey, J. S., et al. (2009). What causes southeast Australia's worst droughts? *Geophysical Research Letters*, 36, L04706. <https://doi.org/10.1029/2008gl036801>

Ummenhofer, C. C., Schwarzkopf, F. U., Meyers, G., Behrens, E., BIASSTOCH, A., & Boning, C. W. (2013). Pacific Ocean contribution to the asymmetry in eastern Indian Ocean variability. *Journal of Climate*, 26(4), 1152–1171. <https://doi.org/10.1175/jcli-d-11-00673.1>

Ummenhofer, C. C., Sen Gupta, A., Briggs, P. R., England, M. H., McIntosh, P. C., Meyers, G. A., et al. (2011). Indian and Pacific Ocean influences on southeast Australian drought and soil moisture. *Journal of Climate*, 24(14), 1313–1336. <https://doi.org/10.1175/jcli-d-11-00229.1>

Ummenhofer, C. C., Sen Gupta, A., England, M. H., Taschetto, A. S., Briggs, P. R., & Raupach, M. R. (2015). How did ocean warming affect Australian rainfall extremes during the 2010/2011 La Niña event? *Geophysical Research Letters*, 42(22), 9942–9951. <https://doi.org/10.1002/2015gl065948>

- Ummenhofer, C. C., Sen Gupta, A., Li, Y., Taschetto, A. S., & England, M. H. (2011). Multi-decadal modulation of the El Niño-Indian monsoon relationship by Indian Ocean variability. *Environmental Research Letters*, 6(3). <https://doi.org/10.1088/1748-9326/6/3/034006>
- Yang, D., Arblaster, J. M., Meehl, G. A., England, M. H., Lim, E.-P., Bates, S., & Rosenbloom, N. (2020). Role of tropical variability in driving decadal shifts in the Southern Hemisphere summertime eddy-driven jet. *Journal of Climate*, 33, 5445–5463. <https://doi.org/10.1175/JCLI-D-19-0604.1>
- Zhang, L., Han, W., Karnauskas, K. B., Meehl, G. A., Hu, A., Rosenbloom, N., & Shinoda, T. (2019). Indian Ocean warming trend reduces GRL Pacific warming response to anthropogenic Greenhouse Gases: An interbasin thermostat mechanism. *Geophysical Research Letters*, 46, 10882–10890. <https://doi.org/10.1029/2019gl084088>
- Zhao, S., Jin, F. F., & Stuecker, M. F. (2019). Improved predictability of the Indian Ocean Dipole using seasonally modulated ENSO forcing forecasts. *Geophysical Research Letters*, 46(16), 9980–9990. <https://doi.org/10.1029/2019gl084196>